PHILOSOPHICAL TRANSACTIONS OF **THE ROYAL SOCIETY** A

MATHEMATICAL, PHYSICAL & ENGINEERING SCIENCES

Motion of a Granular Avalanche in a Convex and Concave Curved Chute: Experiments and Theoretical Predictions

Ralf Greve and Kolumban Hutter

Email alerting service	Receive free email alerts when new articles cite this article - sign up in the box at the top right-hand corner of the article or click **here**

Motion of a granular avalanche in a convex and concave curved chute: experiments and theoretical predictions†

By Ralf Greve and Kolumban Hutter

Department of Mechanics, Technological Institute, Hochschulstr. 1,
DW-6100 Darmstadt, F.R.G.

Contents

This paper deals with the theoretical-numerical and experimental treatment of two-dimensional avalanches of cohesionless granular materials moving down a confined curved chute. Depth-averaged field equations of balance of mass and linear momentum as prescribed by Savage & Hutter (1991) are used. They describe the temporal evolution of the depth averaged streamwise velocity and the distribution of the avalanche depth and involve two phenomenological parameters, the internal angle of friction, ϕ, and the bed friction angle, δ, both as constitutive properties of Coulomb-type behaviour. The equations incorporate weak to moderate curvature effects of the bed.

Experiments were carried out with different granular materials in a chute with partly convex and partly concave curved geometry. In these experiments the motion of the granular avalanche is followed from the moment of release to its standstill by using high speed photography, whence recording the geometry of the avalanche as a function of position and time. Two different bed linings, drawing paper and no. 120 SIA sandpaper, were used to vary the bed friction angle, δ. Both, the internal

† Dedicated to Professor D. Vischer on the occasion of his sixtieth birthday.

angle of friction, ϕ, and the bed friction angle, δ, were measured, and their values used in the theoretical model. Because of the bump and depending upon the granulate–bed combination an initial single pile of granular avalanche could evolve as a single pile throughout its motion and be deposited above or below the bump in the bed; or it could separate in the course of the motion into two piles which are separately deposited above and below the bump.

Comparison of the experimental findings with the computational results proved to lead to good to excellent correspondence between experiment and theory. Even the development of the detailed geometry of the granular avalanche is excellently reproduced by the model equations, if $\delta < \phi$. Occasional deviations may occur; however, they can in all cases be explained by onsetting instabilities of the numerical scheme or by experimental artefacts that only arise when single particles have shapes prone to rolling.

1. Introduction

In the past few years new mathematical descriptions for the motion of rockslides, sturzstroms, and ice and snow avalanches have been presented. Savage & Hutter (1989, 1991) have modelled such motions by the flow of a finite mass of deforming granular materials in flat and weakly curved chutes. They assume an incompressible cohesionless granular fluid model with Mohr–Coulomb-type plastic yield that is expressed by a constant angle of internal friction and suppose a Coulomb dry friction law for the basal sliding in which the shear stress at the bottom is related to the normal stress by a constant friction angle. They derived dynamical equations for the height of the granular pile and the depth averaged longitudinal velocity and predict the spatial and temporal evolution of these fields with numerical finite difference integration schemes. These solutions were determined from an initial profile at rest; rear end and front end positions and, in isolated cases, positions of maximal depth of the moving and deforming piles were followed through time from initiation to runout. For flows in chutes having an inclined leg, a curved part and a horizontal leg for runout (Savage & Hutter 1991; Hutter *et al.* 1992; Hutter 1991) and for flows in exponentially curved chutes (Hutter & Koch 1991) the theoretical fields were in satisfactory agreement with laboratory experiments. However, these results were still challenged by avalanche practitioners, the argument being that agreement between theoretical predictions and laboratory experiments might be less satisfactory in chutes with a convex curved 'bump'. In these cases, depending upon internal and basal friction coefficients a single initial mass of granular material might settle in one of the following three forms: (i) deposition of all the material above the bump, (ii) deposition of all material below the bump, and (iii) splitting of the entire mass in two depositions, one above and the other below the bump. The purpose of this paper is to rebut the conjecture and to demonstrate excellent agreement between theoretical predictions and observations in the laboratory.

In ensuing developments we shall partly rely on the earlier work by Hutter & Koch (1991); however, we try to keep this text as independent as possible. In the following paragraph we present the governing equations but do not derive them. §3 describes the experimental set-up, while §4 gives the numerical integration schemes; it is in this paragraph where sensitivity studies of the system of equations disclose important inferences regarding the role of the internal angle of friction, ϕ, and the
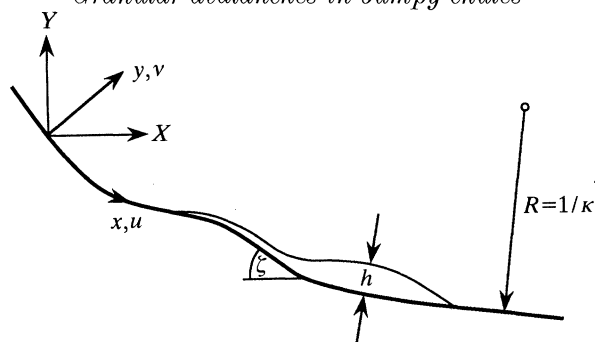
Figure 1. Definition sketch of coordinate system and geometry of a finite mass of granular material moving down a rough curved rigid bed; x and y are dimensionless. ζ is the bed inclination angle, κ the curvature of the bed.

bed friction angle, δ. A comparison of the theoretical findings with the experiments is given in §5. It primarily involves the temporal evolution of the position of the rear end, x_r, the leading edge (front), x_f, the position where the maximal avalanche height, h_s, arises, x_s, and the corresponding value for h_s. The computed and experimentally determined volumina of the deposition(s) are also compared. Finally, we perform a detailed comparison of the evolving avalanche profile for two experiments and demonstrate thereby how excellently the theory reproduces the laboratory experiments. We close in §6 with a summary.

2. Governing equations

We shall study free surface flow of a granular material along a weakly curved profile (see figure 1). The motion is two dimensional, taking place in vertical planes; the pile of the granular material may start from its rest position and flow down the rough bed until it settles in the runout zone. The bed has a steep slope at the initial position of the pile, flattens out in an intermediate region, becomes steeper again beyond this zone and gradually approaches a horizontal flat in the downstream direction. Because of the intermediate bump the finite mass of granular material that is released close to the upper end of the chute may settle either before the bump or behind the bump or else may split and settle partly before and partly behind the bump with proportions that depend on total volume and the frictional properties between the particles themselves and that of the particles and the bed.

Although the material is made up of discrete granules, the body will be treated as a continuum which implies that the thickness, h, of the sliding and deforming body extends over several particle diameters. Moreover, we shall ignore variations of the density due to void ratio and therefore suppose the incompressibility assumption to be valid to a sufficient degree of accuracy. Observations of our laboratory avalanches through the glass side of the confining channel showed variations in overall average bulk density from the initiation of motion until the material comes to rest that are typically less than 20 %. We also assume and have constructed the chute accordingly, that the bump is sufficiently gently curved that lift-off of the granules from the bed does not occur.

Our model equations are based on the following physical statements:

(1) balance laws of mass (in the form of the continuity equation) and linear momentum;

(2) kinematic equation and stress-free boundary conditions at the free evolving surface;

(3) tangency condition of the velocity vector at the basal surface;

(4) constitutive postulates for the material response inside the granular pile and for the sliding mechanism at the bed.

The detailed presentation of these statements has been given by Savage & Hutter (1989, 1991), here we only give a brief account and explain the constitutive behaviour. As for sliding, a simple Coulomb-like dry friction law relates S, the shear traction at the bed, to the normal stress N, through a local friction angle δ, i.e.

$$S = \pm N \tan \delta, \tag{2.1}$$

where the sign is given by the direction of the sliding velocity. Similarly, if the granular material is postulated to obey a Mohr–Coulomb plastic behaviour with a cohesionless yield, then this yield occurs on a surface element if the shear stress, S, and normal stress, N, acting on this element are related by

$$|S| = N \tan \phi, \tag{2.2}$$

where ϕ is the internal friction angle. Justification of these laws for cohesionless granular materials is amply demonstrated by Savage & Hutter (1989).

On the basis of the laws (2.1) and (2.2) it can be shown with the aid of Mohr-circle arguments that longitudinal pressure components p_{xx}, and corresponding pressures, p_{yy}, perpendicular to the sliding surface at the bed are related by

$$p_{xx} = K_{\text{actpass}} \, p_{yy} \quad \text{(at bed)}, \tag{2.3}$$

where
$$\left. \begin{array}{c} K_{\text{act}} \\ K_{\text{pass}} \end{array} \right\} = \left[\frac{2(1 \mp \sqrt{(1 - \cos^2 \phi / \cos^2 \delta)})}{\cos^2 \phi} - 1 \right], \quad \begin{cases} \partial u / \partial x > 0, \\ \partial u / \partial x < 0, \end{cases} \tag{2.4}$$

is the active and passive earth pressure coefficient. The *active*, smaller longitudinal pressure arises when the flow is locally extensional, the *passive*, larger longitudinal pressure occurs when the flow is locally compressive.

In ensuing developments equations will be written in dimensionless form. Thus, different length scales, the longitudinal length scale, L, the depth scale, H, and a scale for the radius of curvature of the bed profile, R, will be used. With these, three different (independent) parameters arise, namely the *aspect ratio*, $\epsilon = H/L \ll 1$, a dimensionless characteristic curvature, $\lambda = L/R$, and the bed friction angle, δ. The following orders of magnitude will be used (Savage & Hutter 1991): $\tan \delta = O(\epsilon^{\frac{1}{2}})$, $\lambda = O(\epsilon^{\frac{1}{2}})$.

Using the local balance laws of mass and momentum in curvilinear orthogonal coordinates as suggested by x- and y-coordinates in figure 1 and integrating these over depth, Savage & Hutter (1991) show that in dimensionless form

$$\frac{\partial h}{\partial t} + \frac{\partial (h \bar{u})}{\partial x} = 0, \tag{2.5}$$

$$\frac{\mathrm{d}\bar{u}}{\mathrm{d}t} = \frac{\partial \bar{u}}{\partial t} + \bar{u} \frac{\partial \bar{u}}{\partial x} = \sin \zeta - \tan \delta \, \mathrm{sgn}\,(\bar{u})\,(\cos \zeta + \lambda \kappa \bar{u}^2) - \epsilon K_{\text{actpass}} \cos \zeta \frac{\partial h}{\partial x} \tag{2.6}$$

must hold, in which all quantities are dimensionless and $\bar{u}$ is the depth averaged

streamwise velocity component. Lengths and depths have been made dimensionless by L and H, respectively, and the velocity scale is $\sqrt{(gL)}$. The dimensional counterpart of (2.6) would be

$$\rho \frac{\mathrm{d}\bar{u}}{\mathrm{d}t} = \rho \left(\frac{\partial \bar{u}}{\partial t} + \bar{u} \frac{\partial \bar{u}}{\partial x} \right)$$

$$= \rho g \sin \zeta - \tan \delta \, \mathrm{sgn} \, (\bar{u}) \, (\rho g \cos \zeta + \rho \bar{u}^2/R) - K_{\mathrm{actpass}} \frac{\partial}{\partial x} (\tfrac{1}{2}\rho g h^2 \cos \zeta). \quad (2.7)$$

The depth-averaged continuity equation (2.5) and the streamwise momentum equation (2.6) or (2.7) involve approximations to the extent that terms of higher order than ϵ have been ignored. Equations (2.6), (2.7) express a balance of acceleration (left-hand side) with the streamwise components of the forces (right-hand side). The first term on the right is the contribution of gravity; the second is the basal friction force consisting of the contribution due to overburden and centrifugal force and the third term is a longitudinal pressure gradient due to depth variations of the pile.

Provided the friction angle, δ, between the avalanche and the bed and the basal geometry (in terms of the bed slope, ζ, and the curvature, κ) are known, the temporal evolution of h and $\bar{u}$ can be determined if an initial profile $h(x,0) = h_0(x)$ and depth-averaged velocity distribution $\bar{u}(x,0) = \bar{u}_0(x)$ are prescribed.

When either $\tan \delta$ or λ or both are smaller than order $\epsilon^{\frac{1}{2}}$ and when $\bar{u}$ does not become too large, then the term in equation (2.6) due to the centrifugal effects may be dropped in comparison with the other terms. This does not mean that effects of the curvature of the bed are ignored in this case since ζ may still vary with position and thus incorporate some weak curvature effects implicitly.

3. Experimental set-up

In this section, the laboratory test apparatus and the experimental procedures will be described. Only a brief description will be given as the procedure follows closely that of Hutter & Koch (1991) and details can be taken from there and from Greve (1991).

(a) The laboratory test apparatus

Experiments were performed in a 100 mm wide chute of variable length somewhat greater than 4000 mm. The basal surface of the chute was made of a flexible strip of a soft plexiglass. This bed could be formed to follow the trace of a prescribed function, in our case the function listed below as equation (3.2a).

This strip was mounted on a vertical plywood wall that was coated by an offwhite plastic folio. The front wall of the arrangement was made of clear and transparent plexiglass through which the moving granular pile could be photographed. A finite mass of dry granular material was confined by a plate, initially oriented vertical, and released from rest by quickly rotating the confining plate and thus permitting the granular material to move down the incline; for photographs, see Hutter & Koch (1991). The motion of the pile of granular material could be observed through the transparent front wall, and it was video-filmed and photographed by a 50 mm

Table 1. *Material constants of all granular materials*

(d is the mean grain diameter, l_{max} the maximum length of a grain found in a sample of *ca.* 200 particles, ρ_b the bulk density (for densest packing), ρ the true density, δ_{sp} and δ_{dp} the bed friction angles on bed lining sandpaper and drawing paper, ϕ the internal friction angle and k_{wall} the wall friction coefficient.)

granulate	d/mm	l_{max}/mm	ρ_b/(g l^{-1})	ρ/(g l^{-1})	δ_{sp}/deg	δ_{dp}/deg	ϕ/deg	k_{wall}/deg
glass 0	3	3.7	1784 ± 15	2730	24.3 ± 1.0	23.6 ± 1.5	31.0 ± 2.0	9.0 ± 2.0
glass 1	5	5.4	1619 ± 10	2730	21.2 ± 1.0	22.4 ± 1.5	29.0 ± 1.5	11.0 ± 2.0
Vestolen	4	4.0	552 ± 10	540	34.6 ± 2.0	24.7 ± 1.5	37.0 ± 2.0	11.0 ± 2.0
quartz 0	3	5.0	1562 ± 20	2600 ± 150	38.5 ± 1.0	31.1 ± 1.5	44.0 ± 2.5	12.0 ± 2.0
quartz 1	5	8.0	1572 ± 15	2600 ± 150	38.7 ± 2.0	30.9 ± 2.0	43.0 ± 3.0	11.5 ± 2.0
marmor 0	3	5.5	1447 ± 40	2500 ± 200	39.5 ± 2.0	33.6 ± 2.0	47.0 ± 3.0	12.5 ± 2.0
marmor 1	5	8.7	1495 ± 35	2500 ± 200	40.4 ± 2.0	32.5 ± 2.0	46.0 ± 4.0	12.0 ± 2.0

camera with a high-speed motor drive capable of operating at nominally 6, 10 and 14 frames per second, respectively. The distance of the camera from the chute varied from 3.5 to 5 m, depending on the kind of granules that were used. A clock, accurate to 0.01 s was also positioned such that it is visible on the photographs.

The tests were performed with the same seven different sorts of granular materials already reported by Hutter & Koch (1991); (i) nearly spherical glass beads (3 and 5 mm nominal diameter), (ii) plastic particles (Vestolen) of lens-like shape having a diameter of 4 mm and a height of 2.5 mm, (iii) quartz chips of roundish shape (3 and 5 mm nominal diameter) and (iv) two fractions of marmor granules with rougher shapes and the same typical diameters. The material mass densities and the bulk densities corresponding to the densest particle packing were already determined by Hutter & Koch (1991), as were the internal angle of friction, ϕ, and the bed friction angle, δ, measured between the particles and the different bed linings, drawing paper and sandpaper, respectively. The influence of the confining walls of the chute on the bed friction was also determined by replacing the bed friction angle, δ, by the *effective* bed friction angle, δ_{eff}, the two being related by

$$\delta_{eff} = \delta_0 + \epsilon k_{wall} h; \tag{3.1}$$

here ϵ is the aspect ratio, h is the dimensionless depth and k_{wall} the measured correction factor to account for the side wall effects in the bed friction angle, see Hutter & Koch (1991). All these quantities are listed in table 1; their experimental determination is described in detail by Hutter & Koch (1991), whose results have also been verified by Greve (1991) by repeating the corresponding measurements.

(b) *Experimental procedure*

A total of 48 experiments were conducted under the following conditions and by varying the following parameters:

(i) bulk volume of the material at its densest packing: 1.5 and 3.0 l;

(ii) the seven different sorts of granular materials: glass 0 and glass 1, Vestolen (plastic beads), quartz 0 and quartz 1, and marmor 0 and marmor 1;

(iii) basal bed linings consisting of drawing paper and no. 120 SIA sandpaper;

(iv) one particular form of the chute: in the dimensionless coordinate, x, (equal to arc length), the slope angle, ζ, is expressed as

$$\zeta(x) = \zeta_0 e^{-0.1x} + \zeta_1 \xi/(1+\xi^8) - \zeta_2 \exp(-0.3(x+10/3)^2) \tag{3.2a}$$
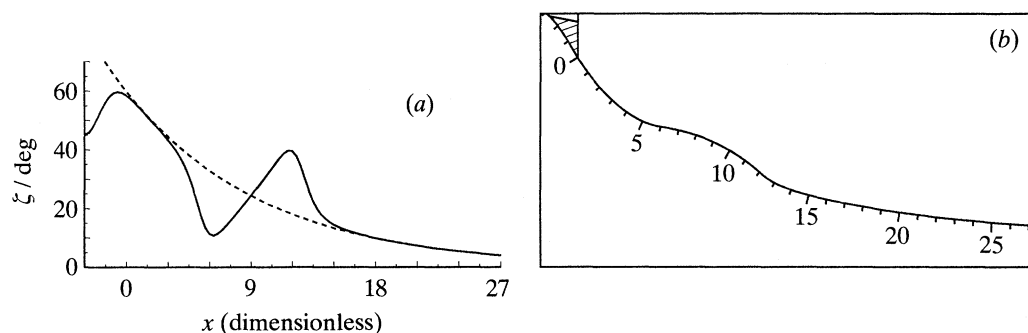
Figure 2. (a) Inclination angle of the chute bed as a function of arc length, x. Dashed is the exponential functional dependence $\zeta = \zeta_0 \exp{(-0.1x)}$ used by Hutter & Koch (1991); the solid line displays the function listed in (3.2). (b) Geometry of the bed of the chute as obtained by the quadratures (3.5) and (3.2). The arc length is reproduced in dimensionless scale. In the upper left corner the initial geometry of an avalanche with volume $V = 3$ l is sketched.

with
$$\xi = \tfrac{4}{15}(x-9) \tag{3.2b}$$

and
$$\zeta_0 = 60.0°, \quad \zeta_1 = 31.4°, \quad \zeta_2 = 37.0°. \tag{3.2c}$$

Here non-dimensionalization has been implemented by choosing for L, H, R 150 mm each. This is legitimate once the reduced equations are derived, provided that the *real* aspect ratio is sufficiently small. The first term in (3.2a) is identical to the bed geometry used by Hutter & Koch (1991), in which ζ_0 corresponds to the initial slope angle; it would yield a bed following an exponentially decaying slope. The second term is responsible for the bump, whence the convex section in the middle of the trajectory. The last term contributes non-negligibly only at the beginning of the trajectory (for $x < 0$); it is flattening the bed in this region to achieve larger volumes behind the gate. This choice is a very accurate representation of the actual bed.

The curvature $\kappa(x) = -\lambda^{-1}\,\mathrm{d}\zeta/\mathrm{d}x$ can readily be deduced from (3.2a),

$$\kappa(x) = -\lambda^{-1}(-0.1\zeta_0\,\mathrm{e}^{-0.1x} + \tfrac{4}{15}\zeta_1(1-7\xi^8)/(1+\xi^8)^2$$
$$+ 0.6\zeta_2(x+\tfrac{10}{3})\exp{(-0.3(x+\tfrac{10}{3})^2)}). \tag{3.3}$$

The minus sign is needed since we take concave curvatures positive by convention. Finally, the bed form in the (X, Y)-coordinate system follows from

$$\mathrm{d}X/\mathrm{d}x = \cos\zeta(x), \quad \mathrm{d}Y/\mathrm{d}x = -\sin\zeta(x), \tag{3.4}$$

by mere integration:

$$X(x) = \int_0^x \cos\zeta(\xi)\,\mathrm{d}\xi + X_0, \quad Y(x) = -\int_0^x \sin\zeta(\xi)\,\mathrm{d}\xi + Y_0, \tag{3.5}$$

in which X_0, Y_0 are the coordinates when $x = 0$. The function $\zeta(x)$ and the bed profile $X(x), Y(x)$ are displayed in dimensionless form in figure 2.

Most experiments were performed twice, once without and once with photographic reproduction, and they were repeated when mechanical or photographic failures occurred. The primary purpose of the first experiment is to obtain estimates for the
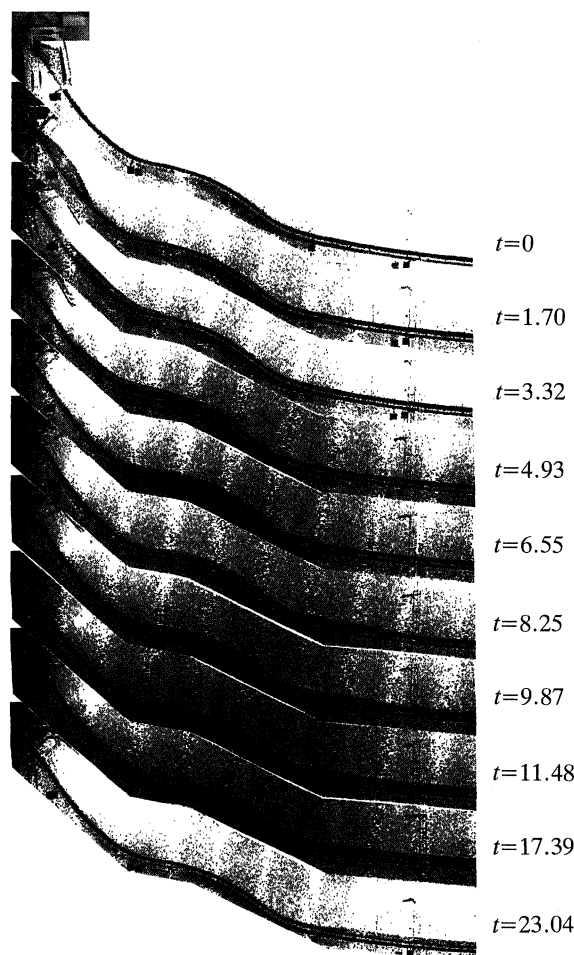
Figure 3. Series of photographs for experiment no. 20 taken at different dimensionless times of 3 l of glass beads (5 mm diameter) on a bed lined with no. 120 SIA sandpaper moving down the chute defined by equation (3.2).

distance of maximal reach and for the duration of the experiment to optimally position the camera. Furthermore, information is obtained this way about the reproducibility of the experiments.

Typical results of test run no. 20 may be seen in figure 3. It shows prints of consecutive shots that are approximately 0.2 s apart of a moving and deforming pile of glass 1-beads on a bed made of no. 120 SIA sandpaper. The photographs document the temporal evolutions of a finite mass of glass beads from the moment of its release to standstill. It is seen that a part of the avalanche cannot at first overcome the bump, thereby forming a 'back' deposition; this deposition, however, is subsequently slowly eroded from its front end, so that eventually only one single 'front' deposition emerges. If the two deposition volumes are denoted by V_r and V_f, respectively, then $V_f/V_r = \infty$ in this case. More frequent has been the case of finite value of V_f/V_r; this means that a finite position of the granular mass is deposited above the bump.

Data of the motion of the avalanche are deduced from projections of the slides of the fast film photographs. In detail, the following quantities are recorded:
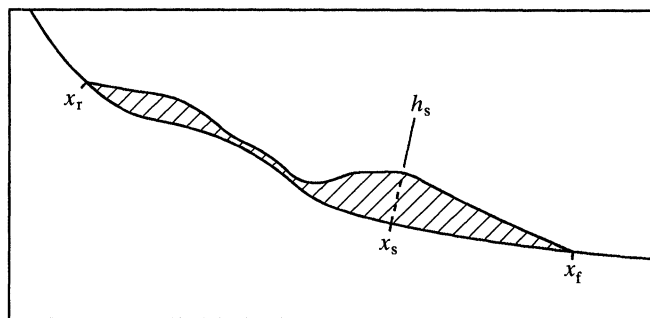
Figure 4. Definition of the geometric parameters x_r, x_f, x_s and h_s of the granular avalanche. The front end, and to a lesser extent also the rear end is often hidden behind a cloud of heavily bouncing particles.

t time of the photograph;

x_r position of the rear end of the avalanche, taken at a position of the bed profile at which the entire width is covered by particles (monolayer coverage);

x_f position of the front end of the avalanche the same as with x_r;

x_s position of that point within the avalanche, where the maximum height is reached;

h_s height at position x_s.

These quantities are defined in figure 4. For the quantities x_r, x_f, x_s and h_s we also determined error bounds. To this end, for each quantity estimates of the inaccuracy for the determination of its value are recorded and thence the absolute errors determined. For x_f these errors become frequently very large, because the avalanche front is often covered by a cloud of bouncing particles which hide the exact position of the front end. Even larger errors arise for x_r in experiments with glass beads shortly before the end of the motion, when the upper deposited mass is slowly eroded from its lower end.

Having determined the positions x_r, x_f at the times when the photographs were taken the velocities of the rear and front ends can be computed as follows:

$$(u_{r/f})_{k+\frac{1}{2}} = [(x_{r/f})_{k+1} - (x_{r/f})_k]/(t_{k+1} - t_k); \qquad (3.6)$$

here the subscript k counts the consecutive photographs. So the time for the computed velocity lies in between the times when photographs were taken. Absolute errors corresponding to the velocities are taken to be

$$\Delta(u_{r/f})_{k+\frac{1}{2}} = \tfrac{1}{4}[\Delta(x_{r/f})_{k+1} + \Delta(x_{r/f})_k]/(t_{k+1} - t_k). \qquad (3.7)$$

The factor $\tfrac{1}{4}$ is inserted to avoid unrealistically large errors; this is reasonable, because it is not justified to incorporate the extent of the entire precursory granular cloud in error estimates for the velocities $u_{r/f}$. More reasonable would be to base the errors in $u_{r/f}$ on inaccuracies of the cloud extents which are distinctly smaller than the total extent of the clouds. We have not done this and introduced the factor $\tfrac{1}{4}$ above instead.

The entire experimental series embraces 48 usable experiments of which 16 were photographically recorded. We varied in these the sort of granular material, the bed lining and the initial volume that was deposited behind the gate and subsequently released. The 16 experiments that were photographed are shown in table 2 together

R. Greve and K. Hutter

Table 2. *List of experiments which were photographically recorded*

(The granular material, the bed lining, the initial volume, V, and x_r, x_f, x_s, h_s (dimensionless) as well as V_f/V_r of the depositions are given. Where two depositions result x_r is the rear end of the pile above the bump and x_f the leading edge of the deposition below the bump.)

| no.	granulate	bed lining	V/l	x_r	x_f	x_s	h_s	V_f/V_r
16	Vestolen	sandpaper	1.5	5.1 ± 0.1	17.4 ± 0.2	6.3 ± 0.3	0.18 ± 0.02	0.523 ± 0.06
17	glass 1	sandpaper	1.5	17.5 ± 0.1	24.8 ± 0.2	18.1 ± 0.3	0.14 ± 0.02	∞
19	Vestolen	sandpaper	3	4.6 ± 0.1	18.8 ± 0.2	5.9 ± 0.2	0.35 ± 0.02	0.574 ± 0.05
20	glass 1	sandpaper	3	16.6 ± 0.1	27.1 ± 0.3	17.2 ± 0.3	0.21 ± 0.02	∞
21	glass 0	sandpaper	1.5	15.5 ± 0.1	23.9 ± 0.3	16.0 ± 0.3	0.16 ± 0.01	∞
22	glass 0	sandpaper	3	14.6 ± 0.1	25.2 ± 0.3	15.3 ± 0.3	0.25 ± 0.02	∞
28	Vestolen	drawing paper	3	4.9 ± 0.1	21.2 ± 0.4	5.9 ± 0.2	0.32 ± 0.01	0.983 ± 0.08
29	Vestolen	drawing paper	1.5	5.7 ± 0.1	20.6 ± 0.4	15.3 ± 0.2	0.13 ± 0.02	1.716 ± 0.27
35	quartz 0	drawing paper	3	4.6 ± 0.1	18.4 ± 0.4	5.9 ± 0.3	0.40 ± 0.02	0.345 ± 0.05
36	quartz 0	drawing paper	1.5	5.3 ± 0.01	17.6 ± 0.4	6.1 ± 0.2	0.23 ± 0.02	0.384 ± 0.08
37	quartz 1	drawing paper	3	4.5 ± 0.1	17.8 ± 0.4	5.8 ± 0.2	0.42 ± 0.02	0.290 ± 0.04
43	glass 0	drawing paper	1.5	17.1 ± 0.1	25.9 ± 0.2	17.6 ± 0.3	0.10 ± 0.02	∞
44	marmor 0	drawing paper	1.5	4.8 ± 0.1	15.3 ± 0.2	6.0 ± 0.3	0.29 ± 0.02	0.0576 ± 0.016
46	marmor 1	drawing paper	1.5	5.1 ± 0.1	15.8 ± 0.2	6.2 ± 0.3	0.24 ± 0.02	0.136 ± 0.04
47	glass 1	drawing paper	1.5	19.1 ± 0.1	?	?	?	∞
48	quartz 1	drawing paper	1.5	5.6 ± 0.1	18.1 ± 0.4	6.5 ± 0.3	0.20 ± 0.02	0.534 ± 0.07
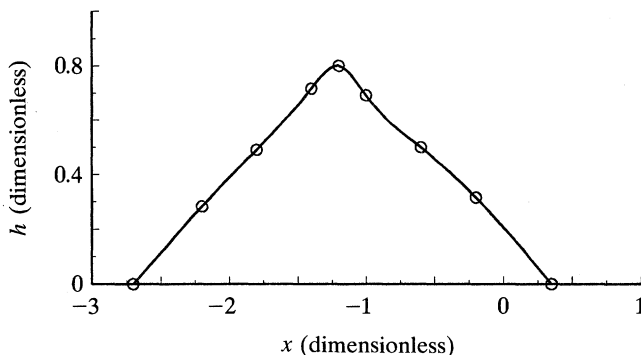
Figure 5. Interpolation by cubic spline for nine measured values of an initial avalanche profile of experiment no. 28.

with data in the deposition area: initial volume, x_r, x_f, x_s, h_s and V_f/V_r. Subsequently we shall refer to this table by simply quoting the experiment number.

(c) *Initial conditions for numerical integration*

In all experiments, the time of the first photograph at which the plate confining the granular material appears to be rotated (off-vertical position) is defined as the temporal origin. The geometry and velocity distribution of the granular mass at this time are used as initial conditions for the subsequent motion. This permits an exact definition of the origin of the time, and allows determination of the geometry and velocity distribution as follows. From the respective slide approximately ten pairs of values for position and height are read off whereby in each case the rear and front end positions are included in order to obtain well-defined boundary points of the avalanche profile. With these values cubic spline interpolation is used to determine the initial geometry, see figure 5; then equidistant cells are defined between the rear and front end,

$$x_i^0 = (x_r)_0 + [(x_f)_0 - (x_r)_0] i/N \quad (i = 0, 1, 2, \ldots, N), \tag{3.8}$$

and corresponding values for the height are determined by the spline interpolated profile.

For the determination of the initial velocity distribution the positions x_r and x_f of the two following slides are also needed. With the aid of these the initial velocities

$$(u_{r/f})_0 = [-3(x_{r/f})_0 + 4(x_{r/f})_1 - (x_{r/f})_2]/2\Delta t + O(\Delta t^2) \tag{3.9}$$

are determined, where $2\Delta t = t_2 - t_0$ and the subscripts 0, 1, 2 enumerate consecutive slides. Equation (3.9) corresponds to a quadratic interpolation. The velocities at the boundaries of the selected cells are now approximately determined by linear interpolation between the rear and front ends, namely

$$\bar{u}_i^{\frac{1}{2}} \approx \bar{u}_i^0 = (u_r)_0 + [(u_f)_0 - (u_r)_0] i/N \quad (i = 0, 1, 2, \ldots, N). \tag{3.10}$$

The superscript is a counting index for time, and the difference between $\bar{u}_i^{\frac{1}{2}}$ and $\bar{u}_i^0$ is ignored. This is acceptable because the superscript refers to the temporal step in the numerical integration, which is much smaller than the time difference between consecutive slides.
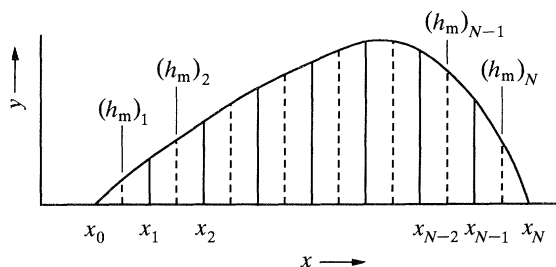
Phil. Trans. R. Soc. Lond. A (1993)

Figure 6. Division of the avalanche volume into material cells for the lagrangian finite difference scheme.

4. Numerical integration scheme

(a) Lagrangian numerical scheme

The following numerical integration routine for the equations (2.5), (2.6) is due to Savage & Hutter (1989, 1991) and has previously been used by Hutter & Koch (1991). The integration scheme is an explicit one-step procedure, by which quantities at time step k (for position and height) and $k + \frac{1}{2}$ (for velocity) are directly computed from corresponding quantities at time step $k-1$ (for position and height) and $k - \frac{1}{2}$ (for velocity). The key idea is to use a material (i.e. lagrangian) net which follows the motion of the avalanche.

The avalanche is subdivided into N material cells, see figure 6. Variables carrying the index m characterize quantities representative for the middle of the cell, those without such an index are typical for the cell boundary. As before, the superscript k counts the time steps as integration goes along.

First, the new positions of the cell boundaries are determined

$$x_i^k = x_i^{k-1} + \bar{u}_i^{k-1/2}\,\Delta t \quad (i = 0, 1, 2, \ldots, N) \tag{4.1}$$

from which the positions of the mid-points of the cells follow to be

$$(x_m)_i^k = \tfrac{1}{2}(x_i^k + x_{i-1}^k) \quad (i = 1, 2, \ldots, N). \tag{4.2}$$

Integrating the mass balance equation (2.5) along the ith cell yields

$$\frac{d}{dt}\int_{x_{i-1}}^{x_i} h\,dx - h(x_i)\frac{\partial x_i}{\partial t} + h(x_{i-1})\frac{\partial x_{i-1}}{\partial t} + h(x_i)\,\bar{u}(x_i) - h(x_{i-1})\,\bar{u}(x_{i-1}) = 0$$

$$(i = 1, 2, \ldots, N) \tag{4.3}$$

from which, since $\bar{u}(x_i) = \partial x_i/\partial t$, we readily deduce

$$\frac{d}{dt}\int_{x_{i-1}}^{x_i} h\,dx = \frac{dF_i}{dt} = 0 \quad (i = 1, 2, \ldots, N), \tag{4.4}$$

where F_i is the area of the ith cell. In other words the area of any materially advected cell is conserved. Approximating F_i by $[(h_m)_i\,(x_i - x_{i-1})]$ $(i = 1, 2, \ldots, N)$, this conservation property implies

$$(h_m)_i^k\,(x_i^k - x_{i-1}^k) = (h_m)_i^{k-1}\,(x_i^{k-1} - x_{i-1}^{k-1}) \quad (i = 1, 2, \ldots, N), \tag{4.5}$$

which determines $(h_m)_i^k$ since all other quantities are known. There remains the computation of the new values of the velocity at the cell centres which can be

determined by means of the momentum equation (2.6). Because $\partial h/\partial x$ terms arise on the right-hand side of (2.6) the boundary cells must be separately handled; the results are

$$\bar{u}_i^{k+\frac{1}{2}} = \bar{u}_i^{k-\frac{1}{2}} + \Delta t\{\sin \zeta_i^k - \tan \delta_i^k \operatorname{sgn}(\bar{u}_i^{k-\frac{1}{2}})(\cos \zeta_i^k + \lambda \kappa_i^k (\bar{u}_i^{k-\frac{1}{2}})^2) - \epsilon \cos \zeta_i^k K_{i\,\mathrm{actpass}}^k$$
$$\times [(h_\mathrm{m})_{i+1}^k - (h_\mathrm{m})_i^k]/[(x_\mathrm{m})_{i+1}^k - (x_\mathrm{m})_i^k] + \Psi_i^k\} \quad (i = 1, 2, \ldots, N-1), \quad (4.6)$$

$$\bar{u}_0^{k+\frac{1}{2}} = \bar{u}_0^{k-\frac{1}{2}} + \Delta t\{\sin \zeta_0^k - \tan \delta_0^k \operatorname{sgn}(\bar{u}_0^{k-\frac{1}{2}})(\cos \zeta_0^k + \lambda \kappa_0^k (\bar{u}_0^{k-\frac{1}{2}})^2)$$
$$- \epsilon \cos \zeta_0^k K_{0\,\mathrm{actpass}}^k (h_\mathrm{m})_1^k/[(x_\mathrm{m})_1^k - x_0^k] + \Psi_0^k\} \quad (i = 0), \quad (4.7)$$

$$\bar{u}_N^{k+\frac{1}{2}} = \bar{u}_N^{k-\frac{1}{2}} + \Delta t\{\sin \zeta_N^k - \tan \delta_N^k \operatorname{sgn}(\bar{u}_N^{k-\frac{1}{2}})(\cos \zeta_N^k + \lambda \kappa_N^k (\bar{u}_N^{k-\frac{1}{2}})^2)$$
$$- \epsilon \cos \zeta_N^k K_{N\,\mathrm{actpass}}^k - (h_\mathrm{m})_N^k/[x_N^k - (x_\mathrm{m})_N^k] + \Psi_N^k\} \quad (i = N), \quad (4.8)$$

in which Ψ_i^k is an artificial diffusive term which must be incorporated to dampen out spurious numerical oscillations, see Anderson *et al.* (1984). Explicitly we choose

$$\Psi_i^k = \mu(\partial^2 \bar{u}/\partial x^2)|_i^k \quad (4.9)$$

and select the discretizations

$$\Psi_i^k = \mu(a_i^k \bar{u}_{i+1}^{k-\frac{1}{2}} + b_i^k \bar{u}_i^{k-\frac{1}{2}} + c_i^k \bar{u}_{i-1}^{k-\frac{1}{2}}) \quad (i = 1, 2, \ldots, N-1), \quad (4.10)$$

$$\Psi_0^k = \mu(a_1^k \bar{u}_2^{k-\frac{1}{2}} + b_1^k \bar{u}_1^{k-\frac{1}{2}} + c_1^k \bar{u}_0^{k-\frac{1}{2}}) \quad (i = 0), \quad (4.11)$$

$$\Psi_N^k = \mu(a_{N-1}^k \bar{u}_N^{k-\frac{1}{2}} + b_{N-1}^k \bar{u}_{N-1}^{k-\frac{1}{2}} + c_{N-1}^k \bar{u}_{N-2}^{k-\frac{1}{2}}) \quad (i = N), \quad (4.12)$$

with

$$a_i^k = \frac{2}{(L_{i+1}^k)^2 + L_i^k L_{i+1}^k}, \quad b_i^k = -\frac{2}{L_i^k L_{i+1}^k}, \quad c_i^k = \frac{2}{(L_i^k)^2 + L_i^k L_{i+1}^k}, \quad L_i^k = x_i^k - x_{i-1}^k.$$

This rather complicated discretization is necessary, since the cell boundaries are not equidistant in general. Incidentally, μ is an artificial (dimensionless) numerical viscosity, values for which are from 0.05 to 0.15 for best numerical performance.

Finally, the active and passive earth pressure coefficient, K_act and K_pass, respectively, are selected, for the cells 1 to $N-1$, according to whether $\bar{u}_{i+1} - \bar{u}_i \gtrless 0$ and, for cell N, according to whether $\bar{u}_N - \bar{u}_{N-1} \gtrless 0$.

(b) *Experiences with computations*

The above numerical integration scheme contains three numerical parameters, the number of cells, N, the temporal integration step, Δt, and the artificial viscosity, μ; at first it expediates to select appropriate values for these. A detailed analysis not shown here (see Greve 1991) revealed that the results are most critically dependent upon values of μ. When $\mu \leqslant 0.02$ numerical computations are likely to become unstable, when $\mu \geqslant 0.4$ the effects of numerical diffusion override the other physical effects. Greve concludes that

$$N = 40, \quad \Delta t = 0.002, \quad \mu = 0.05 \quad (4.13)$$

are appropriate values for routine computations; this corroborates similar earlier findings by Hutter & Koch (1991). Computations are followed through time until $t_\mathrm{end} = 30$ (dimensionless), for which the motion in all experiments has ceased.

The material parameters δ_0, ϕ and k_wall corresponding to a particular granulate

Table 3. *Numerical values in degrees ( )° for the bed friction angle δ_0 as used in the numerical computations*

(Numbers in parentheses list the measured values. Dashes indicate cases for which no experiments were performed.)

granulate	δ_0 (sandpaper)	δ_0 (drawing paper)
glass 0	24 (24.3)	22 (23.6)
glass 1	21 (21.2)	20.5 (22.4)
Vestolen	29 (34.6)	26.5 (24.7)
quartz 0	— (38.5)	30 (31.1)
quartz 1	— (38.7)	29 (30.9)
marmor 0	— (39.5)	33 (33.6)
marmor 1	— (40.4)	32 (32.5)

and bed combination as listed in table 1 are systematically too big, because the measuring technique determines *static* rather than *dynamic* quantities. For the bed lining 'drawing paper', however, a roughening effect can also be observed, the reason being that with ongoing experiments the drawing paper was worn out and the contact becoming rougher; in other words, δ_0 was becoming larger with increasing number of experiments.

The dependence of the numerical results upon variations of ϕ and k_{wall} turned out to be very small; therefore the values for these quantities are taken over from table 1 without any changes. Alternatively, in coincidence with earlier findings by Hutter & Koch (1991), the dependence of the numerical results for avalanche geometry and velocity upon δ_0 is significant; for this reason preliminary computations are conducted in these cases with values of δ_0 in the neighbourhood of the measured values and results compared with the experiments to determine the optimal value of δ_0 for each granulate-bed combination. The results are listed in table 3. Evidently, the values used in the computations are indeed systematically somewhat smaller than the measured static values except for the plastic beads (Vestolen) on 'drawing paper', where abrasion caused a roughening of the bed.

It was also observed that the standard values (4.13) for N, Δt and μ did not permit numerically stable integration for a granular avalanche with initial volume of 3 l (the only exception is when the glass beads are used). The problem could be cured by selecting a smaller cell number ($N = 20$ or even $N = 10$) at the price of a coarser resolution. The choice of smaller time steps Δt led to very long non-economic integration times; neither was an increase of the artificial viscosity μ successful. The problem warrants further study.

Finally, a peculiar numerical trick that was occasionally used ought to be mentioned; it is merely justified by the fact that it works. The problem concerns the physically unrealistic retardation of the last few cells in experiments with glass beads: If the dimensionless length of one of the last three cells exceeds the value 2, then its length is cut in half and its height doubled (to conserve volume). Such cells have always heights which lie below the particle diameters and thus this 'push-forward operation' is physically irrelevant anyhow. However, with it, it cannot be expected that the computed velocity in the rear of the granular avalanche will match corresponding values deduced from experiments.
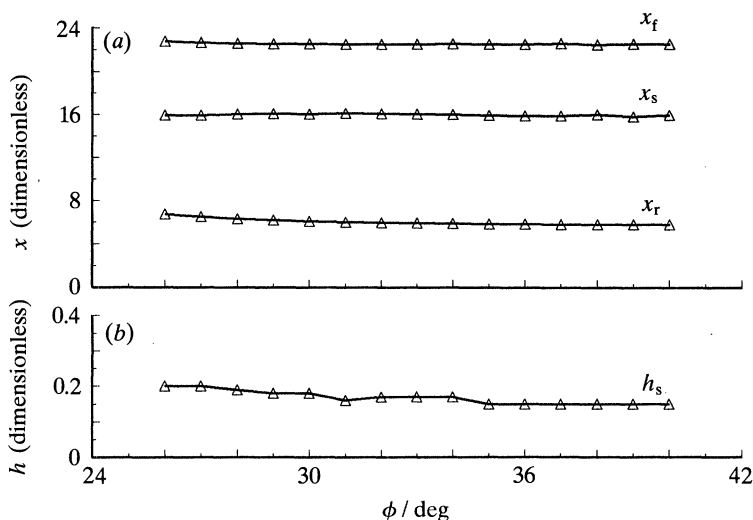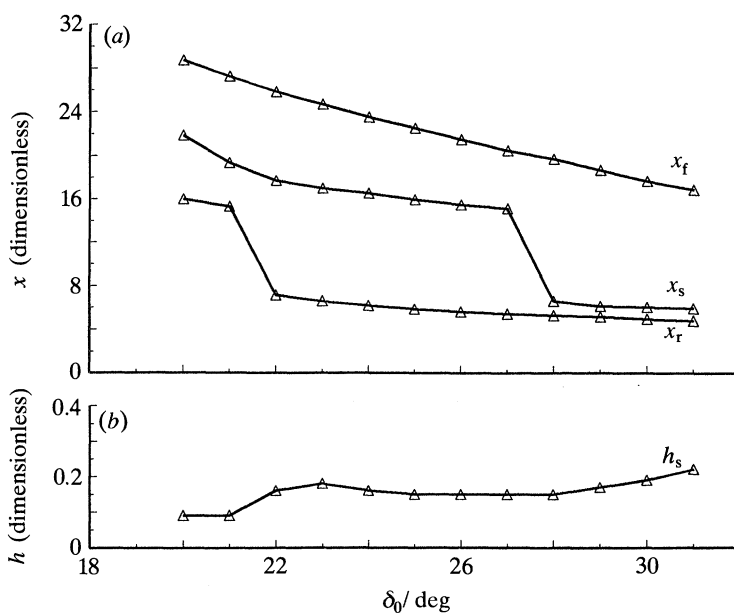
Figure 7. Computed values for x_r, x_f, x_s (a) and h_s (b) of the geometry of the settled avalanche plotted against the internal angle of friction, ϕ, holding the other parameters fixed. $V = 1.5\,\mathrm{l}$, $\delta_0 = 25°$, $K_{\mathrm{wall}} = 10°$, $N = 40$, $\Delta t = 0.01$, $\mu = 0.05$.

Figure 8. Computed values for x_r, x_f, x_s (a) and h_s (b) of the geometry of the settled avalanche plotted against the bed friction angle δ_0, holding $\phi = 35°$ and the other parameters fixed (as in figure 7).

(c) Sensitivity studies

To test the dependence of the model upon the material parameters δ_0 and ϕ, a series of computations was conducted, in which one of the parameters was held fixed, while the other was varied; the setting of experiment no. 36 was used as initial condition. The δ_0-series was computed with δ_0 varying from $20°$ to $31°$ in steps of $1°$ with $\phi = 35°$, $k_{\mathrm{wall}} = 10°$, $N = 40$, $\Delta t = 0.01$ and $\mu = 0.05$; the ϕ-series had ϕ varied
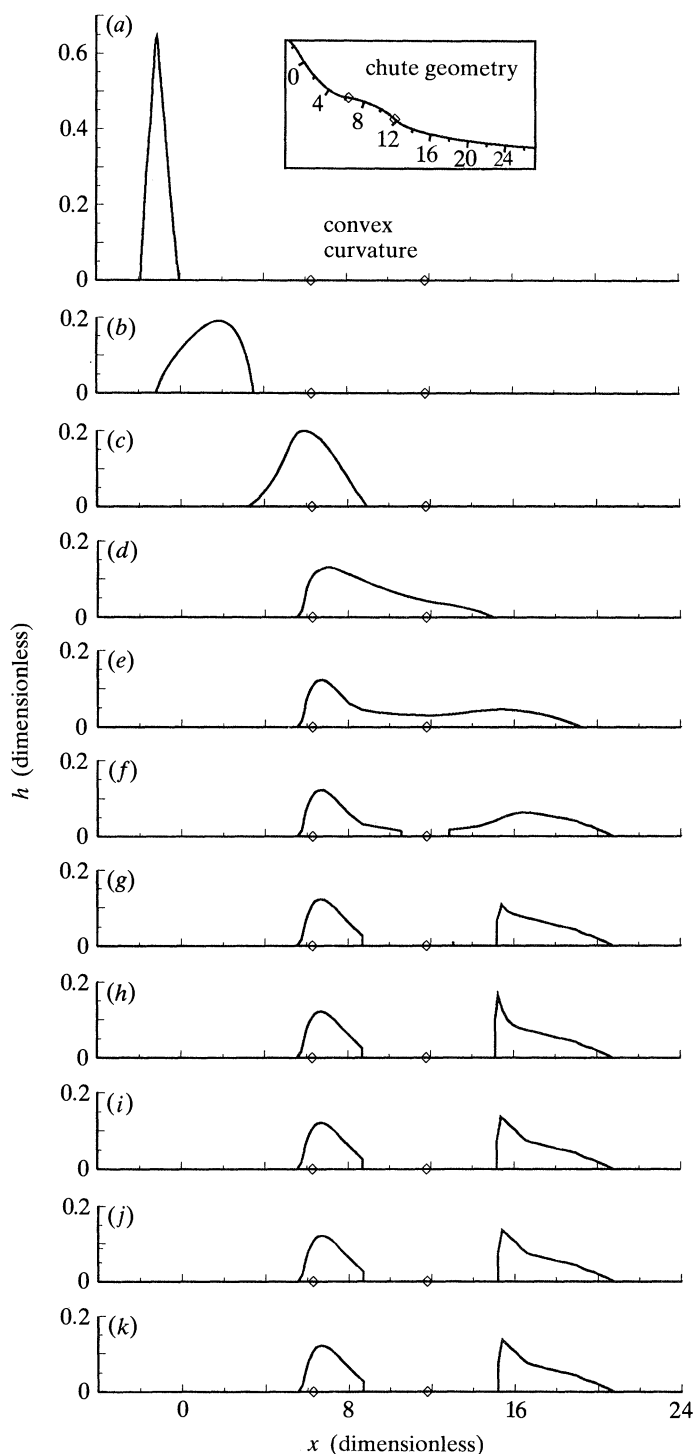
Figure 9. Computed profile of the avalanche height for conditions of exp. 29, each panel representing a 'snapshot' of the geometry at fixed (dimensionless) times with $\Delta t = 3$: (a) $t = 0$, ... (k) $t = 30$. The inset shows the bed geometry together with the (dimensionless) scale along the arc length. This coordinate is unrolled as the horizontal axis in each panel; perpendicular to it the

from 26° to 40° in steps of 1° and $\delta_0 = 25°$, $k_{\text{wall}} = 10°$, $N = 40$, $\Delta t = 0.01$, $\mu = 0.05$ were held constant. We study the dependence of x_r, x_f, x_s and h_s in the rest position of the run-out zone upon δ_0 and ϕ, respectively. Results are summarized in figures 7 and 8. It is seen that the dependence of the mentioned variables upon ϕ is very moderate, as only a small trace of an increase of the avalanche length ($x_f - x_r$) with increasing ϕ can be observed. Accompanied with this is a correspondingly small decrease in height h_s. This mere marginal dependence of the settled avalanche geometry upon ϕ stems from the weak dependence of the governing equations (2.5) and (2.6) upon ϕ; the earth pressure coefficient alone depends upon ϕ, and it arises in a term that is $O(\epsilon)$.

The dependence of the geometry of the settled avalanche upon the bed friction angle, δ_0, is naturally conspicuous (figure 8). The values of the positions of the rear end, x_r, the front end, x_f, and the location of the maximal height, x_s, decrease with increasing δ_0, obviously because the drag resistance of the bed increases with δ_0. Two transitional régimes are interesting to observe. Between $\delta_0 = 21°$ and $\delta_0 = 22°$ x_r suddenly decreases; a similar behaviour is seen for x_s between $\delta_0 = 27°$ and $\delta_0 = 28°$. In the first transition, when $\delta_0 \leqslant 21°$, the entire avalanche traverses the bump and settles below it; for $22° \leqslant \delta_0 \leqslant 27°$, however, the rear end, x_r, settles before the bump has been passed, while the location of the maximum height, x_s, and the front end, x_f, settle below the bump. Here, two depositions are formed. The second transition ($27° < \delta_0 < 28°$), on the other hand, is formed because with increasing δ_0 the magnitude of the rear deposition grows at the costs of the front deposition, until x_s 'jumps' from the front deposition to the rear deposition. The behaviour of h_s agrees with this interpretation. Letting δ_0 decrease from 31° to 28°, h_s correspondingly decreases (x_s lies above the bump and the volume of the corresponding deposition slowly decreases with decreasing δ_0). For $23° \leqslant \delta_0 \leqslant 27°$, however, h_s grows slightly with increasing δ_0, since x_s has jumped from 'behind the bump' to 'in front of the bump'. At small values of $\delta_0 \leqslant 22°$, h_s decreases again with decreasing δ_0, since in this régime the entire avalanche mass has traversed the bump and its deposition becomes longer as δ_0 decreases.

The dynamics of the granular avalanche along the bed with a bump depends to a large extent on initial mass and material parameters: for 1.5 l glass 1 beads on sandpaper (exp. 17) the computational avalanche completely overrides the bump, whereas for 1.5 l glass 0 beads on sandpaper (exp. 21) a small portion of the total mass settles above the bump (in disagreement with the experiment). When 1.5 l Vestolen on a bed lining formed with drawing paper (exp. 29) is used, two depositions of the same order of magnitude are obtained, one above, the other below the bump. Finally, when 1.5 l of marmor 0 chips on drawing paper (exp. 44) is used, most of the computed granular mass is deposited above the bump. Greve (1991) illustrates all these cases graphically. Here we confine ourselves to presenting the computational results for the conditions of exp. 29, see figures 9 and 10, which display the depth and velocity distributions in the form of consecutive 'snapshots'. In the horizontal direction the dimensionless arc length is plotted, and vertically the height and velocity distribution, respectively, for eleven different values of the dimensionless

---

(dimensionless) distribution of the avalanche height is shown. The section of the bed between the two diamond symbols indicates the portion of the bed with convex curvature. Physical and numerical parameters pertinent to the experiment and the computations are $V = 1.5$ l, $\delta_0 = 26.5°$, $\phi = 37°$, $K_{\text{wall}} = 11°$, $N = 40$, $\Delta t = 0.002$, $\mu = 0.05$.
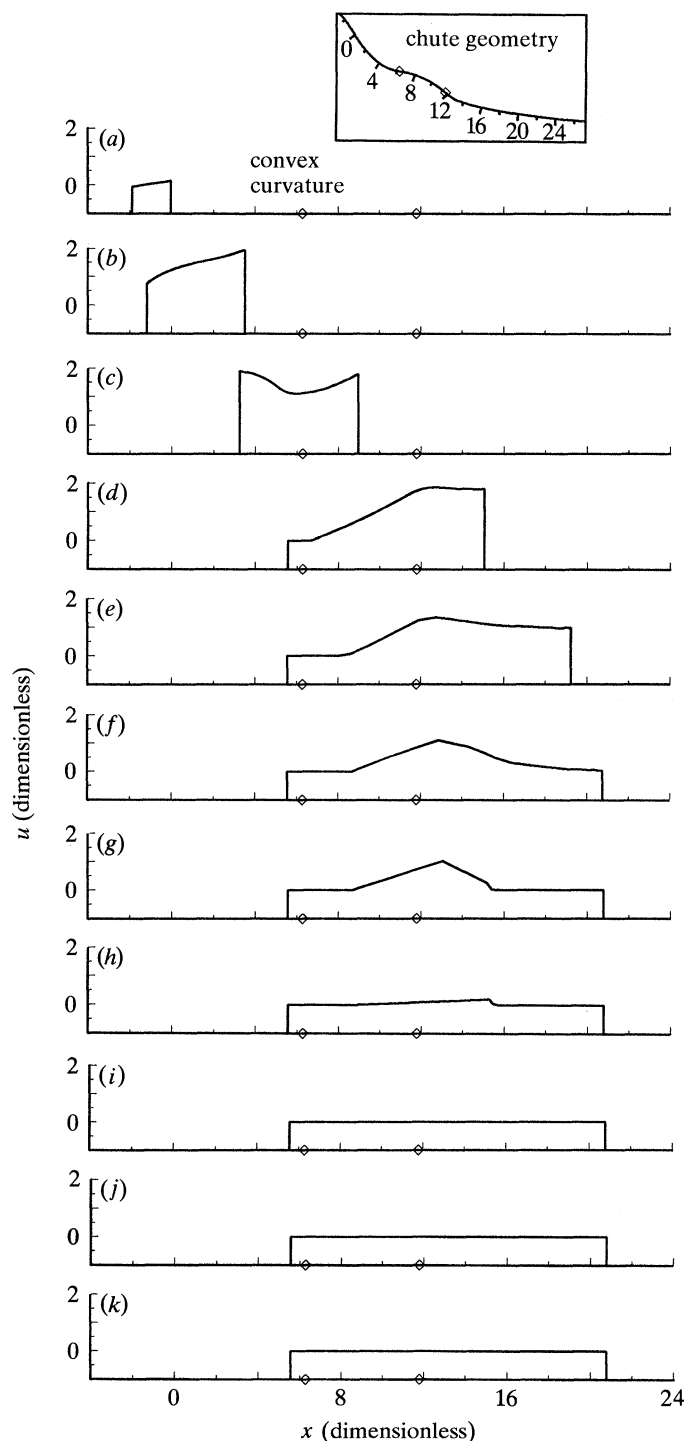
Figure 10. Computed velocity distributions for conditions of experiment no. 29; each panel corresponds to the respective panels in figure 9 and represents a 'snapshot' of the velocity distribution at the indicated (dimensionless) time. Other details are as in figure 9. Compare also with the main text.
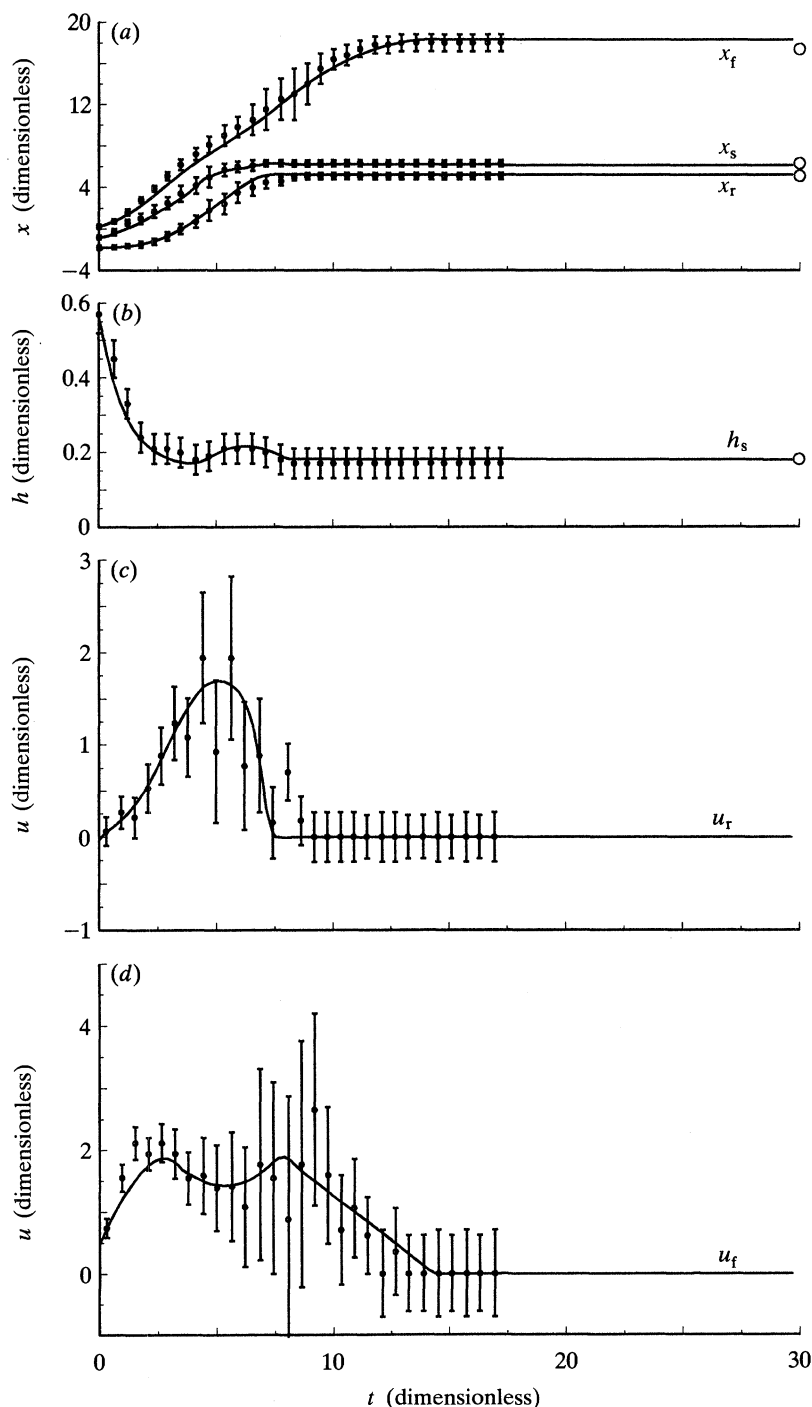
Figure 11. Experimental measurements and computational predictions of x_r, x_f, x_s (a) and h_s (b), as well as velocities u_r (c) and u_f (d) as functions of dimensionless time for experiment no. 16 (1.5 l Vestolen on sandpaper). Data points are shown including errors bars, and values of physical and numerical parameters used in the integration process are (a), (c) $\delta_0 = 29°$, $\phi = 37°$, $K_{wall} = 11°$, $N = 40$, $\Delta t = 0.002$, $\mu = 0.05$. ———, Theory; ϕ, $\circ$, experiment (motion, deposition).

R. *Greve and K. Hutter*
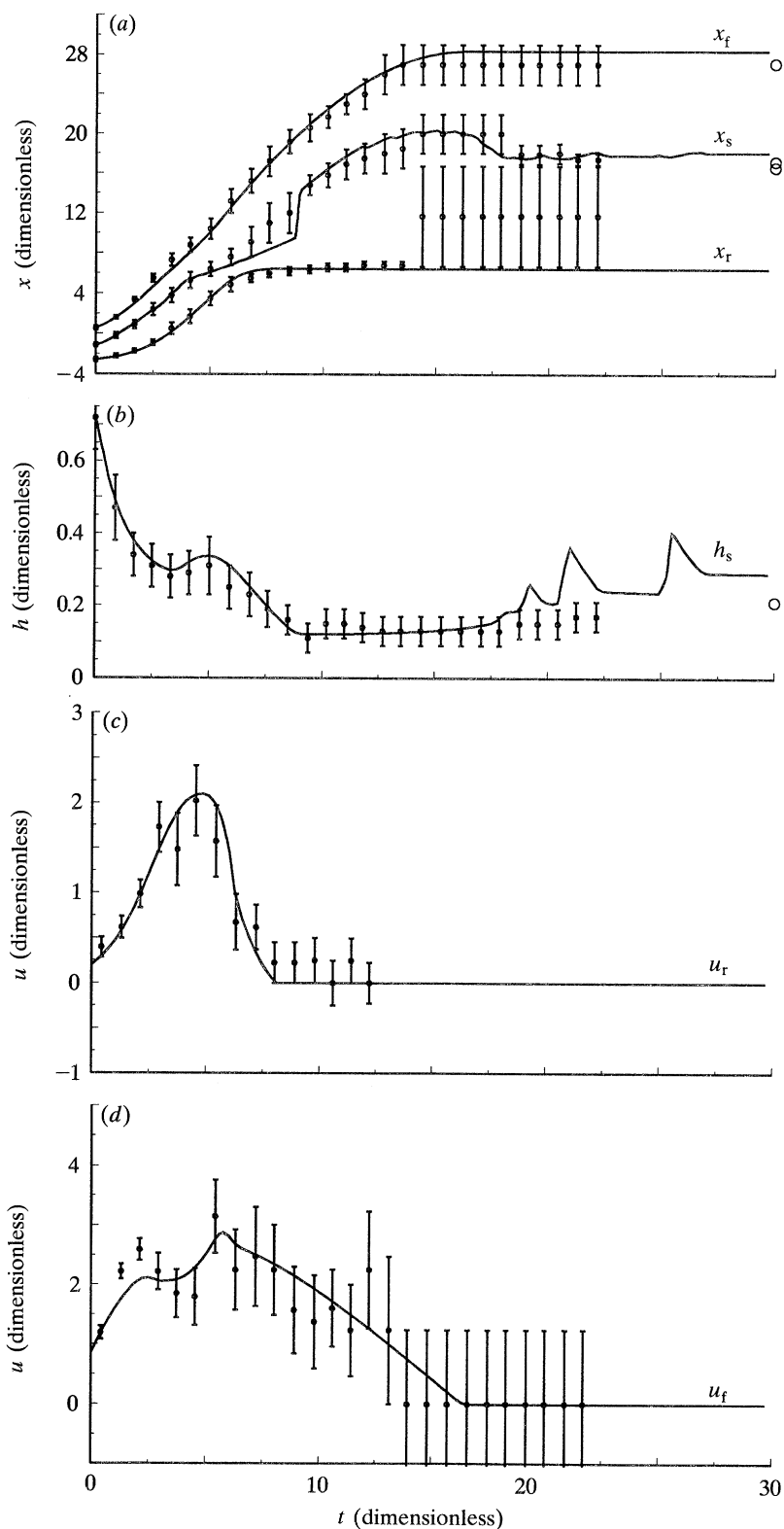
time. The inset figure displays the bed geometry with the length scale corresponding to the unrolled scale of the horizontal axis; the diamond symbols delimit the region of the bump. Shown also are the physical and computational parameters that were used. It is seen that the initial single heap splits in the course of time into two separate, smaller granular masses that settle above and below the bump. Actually, this separation is computationally never obtained, as one can easily infer from equation (4.5); at times $t \geqslant 15$ the computation delivers in the region of the lower part of the bump and immediately below it a cell that is very long with a height much smaller than the particles diameter. These heights are physically irrelevant and have been set to zero when plotting figure 9. In the corresponding velocity plots this artefact has not been implemented which is the reason why the velocity distributions in each panel of figure 10 extend from the rear end of the upper to the front end of the lower moving mass. On the other hand, the extreme elongation of the cells is responsible for the fact that the numerical height and velocity profiles sometimes develop 'kinks' in the vicinity of the bump; the reason is that the model only computes heights and velocities at cell boundaries, and linear interpolation is used in between.

5. Comparison of theoretical results with experiments

In this section we compare some of the numerically determined results with data obtained from experiments.

(a) *Temporal evolution of x_r, x_f, x_s and h_s*

One test of the suitability of the theoretical model is to compare the temporal evolution of the position of the rear end, x_r, the position of the front, x_f, the location where the maximum height arises, x_s, and the height, h_s, at this point; furthermore the velocities of the rear end, u_r, and that of the frontal end, u_f, are compared. We present diagrams in which (dimensionless) x_r, x_f, x_s and h_s are plotted against dimensionless time (see figures 11, 12). Greve (1991) has made comparisons for all 16 experiments for which systematic photographs were taken; here we must confine attention to a selection of results.

Generally, Greve (1991) concludes that the agreement between the numerically and experimentally determined temporal evolutions of the above mentioned quantities is good. The best agreement is obtained for experiment no. 16 (see figure 11) for which practically all experimental values (with their error bars) embrace the corresponding computed values for these variables. A case in which the experimental results appear to be poorly reproduced is experiment no. 20 (see figure 12). Evidently, the computed rear position, x_r, seems to reproduce the experimental counterpart rather poorly. This fact – also observed in all other experiments using glass beads – is due to the more or less distinct rolling of individual beads from the front position above the bump to a new rear position below the bump. The motion of the granular avalanche as a continuum in these cases always ends with two separate positions, one above, the other below the bump. However, because some granules, in particular those of the almost nearly perfectly spherical glass beads,

---

Figure 12. Same as figure 11, but now for experiment no. 20 (3.0 l of glass 1 beads on sandpaper). Physical and numerical parameters used in the integration are $\delta_0 = 21°$, $\phi = 29°$, $K_{\text{wall}} = 11°$, $N = 40$, $\Delta t = 0.002$, $\mu = 0.05$.
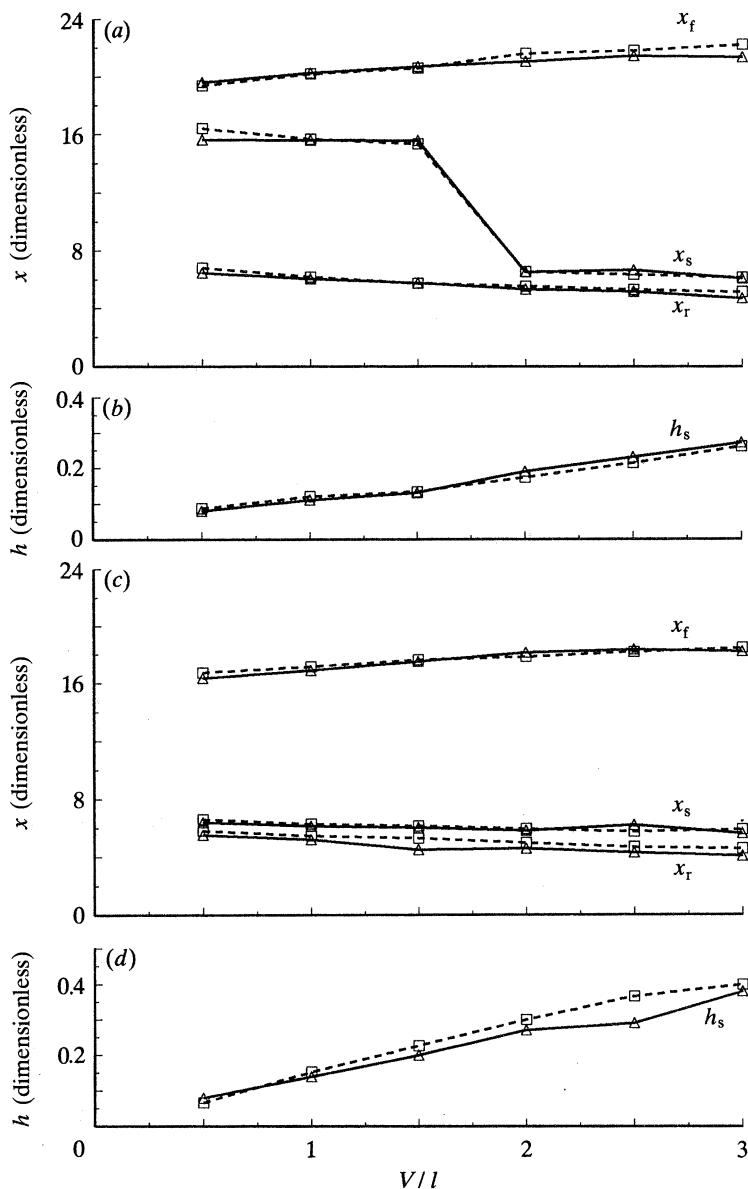
Figure 13. Experimentally (dashed lines) and computationally (solid lines) determined values for x_r, x_t, x_s and h_s as functions of the volumes. Panels (a) and (b) are for 'Vestolen on drawing paper', panels (c) and (d) for 'quartz 0 on drawing paper'. (a), (c) $\delta_0 = 26.5°$, $\phi = 37°$, $K_{wall} = 11°$; (c), (d) $\delta_0 = 30°$, $\phi = 44°$, $K_{wall} = 12°$; (a)–(d) $N = 20$, $\Delta t = 0.001$, $\mu = 0.05$. (b), (d) □----□, Experimental deposition; △—△, theoretical deposition.

start to roll at inclination angles much smaller than the bed friction angle δ_0, the motion in the experiments does not come to rest; rather, the front end of the deposition above the bump is eroded and continuously deposited at the rear end of the lower deposition (drizzling effect). In all experiments with glass beads this process continues until a single deposition below the bump is reached. Incidentally,

Phil. Trans. R. Soc. Lond. A (1993)

this fact explains why the determination of the position of the rear end, x_r, close to run out is associated with large errors.

As is evident from figure 12, the computational prediction of x_f, x_s, h_s and u_r is good; that of x_r does not properly reproduce the rolling of individual beads, but this can be no surprise once the above explanations have been given. Furthermore, towards the end of the motion the computed h_s shows occasional peaks; we have not been able to explain these peaks, however since they relax very quickly, a special cure does not seem to be mandatory. Finally, it is interesting that u_r is well reproduced, while u_f seems to be less. Furthermore, it is worthy to note that x_s, when it is positioned in the lower frontal deposition (which it is in figure 12 and all experiments with glass beads), goes through a relative maximum and tends, towards the cessation of the motion, again to smaller values; this behaviour is accompanied with a slight increase of h_s. Both behaviours are (qualitatively) correctly predicted by the theory. This too is the result of the drizzling of the rolling particles; for by this motion, which adds granules to the rear end of the frontal deposition, x_s must move backwards and h_s must increase. Since the drizzling process does not occur with granular materials other than glass beads, this increase in height is not observed in those cases.

(b) *Volume of deposits*

In what follows we compare the volumina of the rear and frontal depositions as obtained from the computations and determined by experiment. To this end table 4 lists the ratios, V_f/V_r, of the volumes of the frontal deposition to that behind it (rear) for all 16 experiments in which photographs were taken. The experimental volumes are recorded by directly measuring the volumes of the two deposition piles after each experiment, whereas the theoretical volumes are determined by numerical quadrature of the computed profiles at rest. It is seen from table 4 that with one exception all experimental values of V_f/V_r are larger than their theoretical counterparts, whereby differences are particularly large for experiments with 3 l total volume, but nearly within the listed error bounds for experiments with 1.5 l total volume. This can be explained, since for the 3 l experiments stable numerical integration was only achieved with a small cell number ($N = 10, 20$) which makes the determination of the volumes relatively inaccurate. The systematic difference is certainly the effect of drizzling which leads to larger experimental volumes in the frontal deposition than can be obtained computationally where drizzling is absent. This effect is particularly conspicuous in experiments no. 20, 21 and 22.

We have also studied the essentials of the behaviour of the depositions for a fixed granulate-bed combination, but for different volumes. To this end the combinations 'Vestolen/drawing paper' and 'quartz 0/drawing paper' are considered; experiments were conducted and computations performed for masses having the volumes 0.5 l, 1.0 l, ..., 3.0 l. The rest positions x_r, x_f and x_s and the heights h_s are displayed in figure 13. The coincidence between experiments and theory is excellent including such details as the transition of x_s from the front deposition the rear deposition for $1.5 \, l < V < 2.0 \, l$ in figure 13a.

(c) *Detailed comparison for experiments no. 29 and 36*

In particular, a comparison of the experimentally determined avalanche geometries at the times when the snapshots were taken is made with corresponding computed avalanche geometries. The results of these studies are summarized in
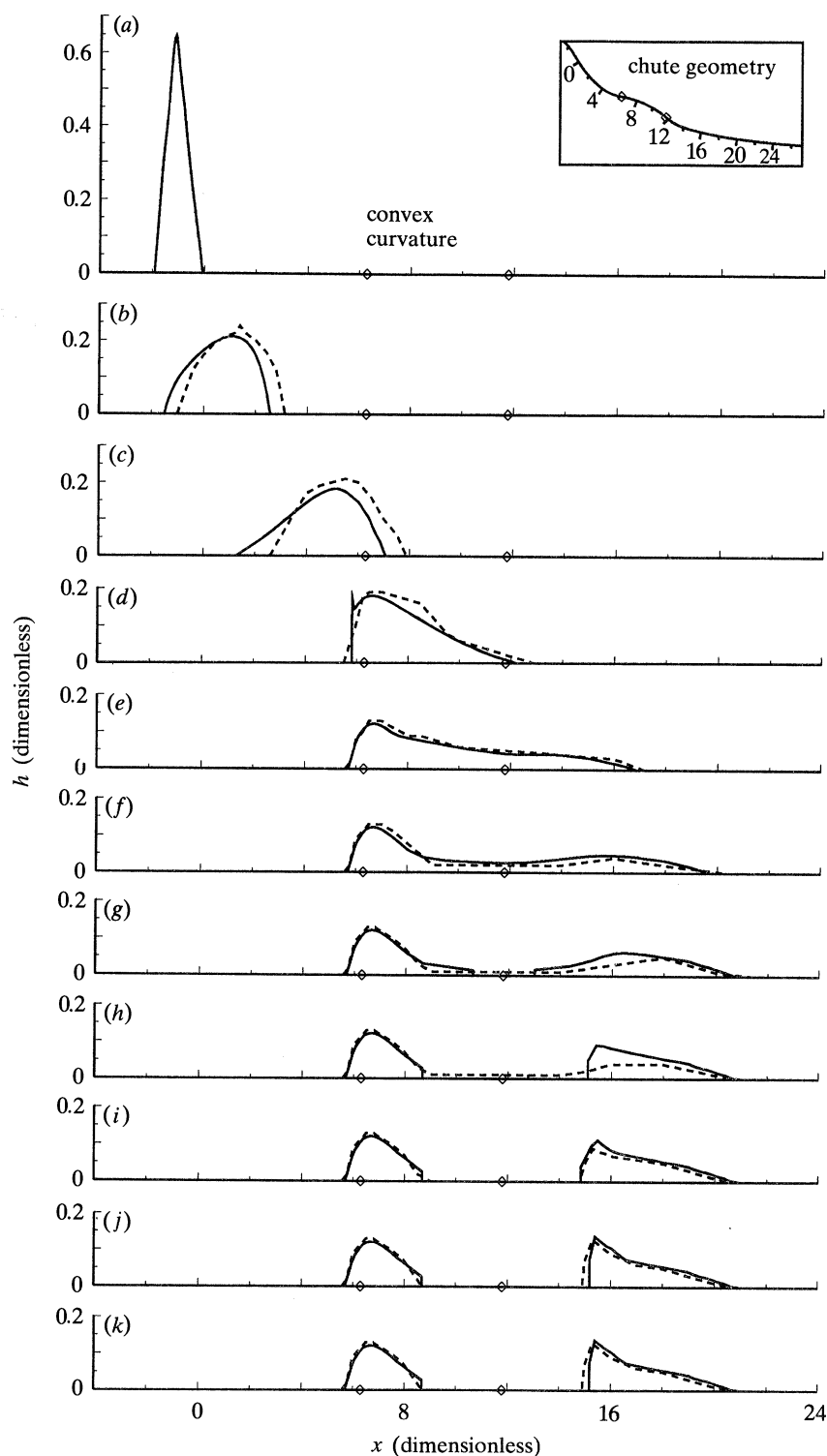
R. *Greve and K. Hutter*

Figure 14. Experimentally determined (dashed) and computed (solid) avalanche profiles for experiment no. 29 (1.5 l of Vestolen on drawing paper; $\delta_0 = 26.5°$, $\phi = 37°$, $K_{wall} = 11°$, $N = 40$,

figures 14 and 15. Evidently, in both cases excellent agreement between theory and experiment is obtained. Deviations are generally within the error bounds that are associated with the experimental data, however, these bounds are not shown in the figures in order not to overload them. It is noteworthy, that the model computations reflect for all times of the experimental duration the measured avalanche profiles surprisingly well, including such details, as the profile shapes and the separation of the single granular masses into two separate piles. In experiment no. 29 (figure 14) a trace of numerical instability can, perhaps, be discerned, however, it does not further develop and quickly relaxes.

In summary the chute flow of a cohesionless granular material along a bed topography with convex and concave curved segments is well predicted by the Savage–Hutter equations (2.5) and (2.6). The deviations of the theoretical predictions from the corresponding experimentally deduced results are in most cases small; occasional larger discrepancies can, in general, qualitatively be explained to a sufficient degree of satisfaction and can often be traced to the before mentioned drizzling effect.

6. Concluding remarks

In this paper we have presented a comparison of results obtained with laboratory experiments on the motion of a finite mass of a cohesionless granular material down a curved bed with convex and concave curved segments with computational predictions as obtained with the theoretical model of Savage & Hutter (1989, 1991). The analysis is based upon depth-averaged conservation of mass and linear momentum equations and the assumptions of material incompressibility, small depth-to-length ratio of the pile, small to moderate bed curvature, and a simple Coulomb-like constitutive behaviour both for the interior of the granular material and for bed friction. Experiments were performed with different granular materials and different bed linings to permit an analysis of the avalanche motion for a large range of values for the internal and bed friction angles. Experiments were conducted for a 100 mm wide chute whose bed was essentially exponentially curved, but had superposed on it a segment with convex curvature to generate a bump. The motion of a finite mass (either 3 l or 1.5 l) of the granular material from initiation to runout along this curved bed was photographed with a fast speed camera and occasionally also video-filmed, and from this information the temporal evolutions of the rear end, x_r, the leading edge, x_f, and the position x_s where the maximum height arises, including this height, h_s, were inferred as were the velocities at the rear end, u_r, and at the front end, u_f.

Numerical solutions for the evolution of the geometry of the avalanche as it is released from rest, moves down the slope and eventually comes to rest, perhaps as a single heap above or below the bump, or else, in two separate depositions above and below the bump, were obtained by a lagrangian finite difference approximation of the governing equations, that was already successfully used by Savage & Hutter (1989, 1991) and Hutter & Koch (1991). The general evolution of the moving and deforming pile from an initial profile with prescribed velocity distribution was followed through

---

$\Delta t = 0.002$, $\mu = 0.05$), each panel representing a 'snapshot' of the geometry at fixed (dimensionless) times in time steps $\Delta t \approx 2.5$: (*a*) $t = 0$; (*b*) $t = 2.5$; (*c*) $t = 4.93$; (*d*) $t = 7.60$; (*e*) $t = 10.10$; (*f*) $t = 12.53$; (*g*) $t = 15.12$; (*h*) $t = 17.71$; (*i*) $t = 20.21$; (*j*) $t = 22.80$; (*k*) $t = 25.39$. The inset figure shows the bed geometry together with the (dimensionless) scale along the arc length. Otherwise reproduction is the same as in figure 9.
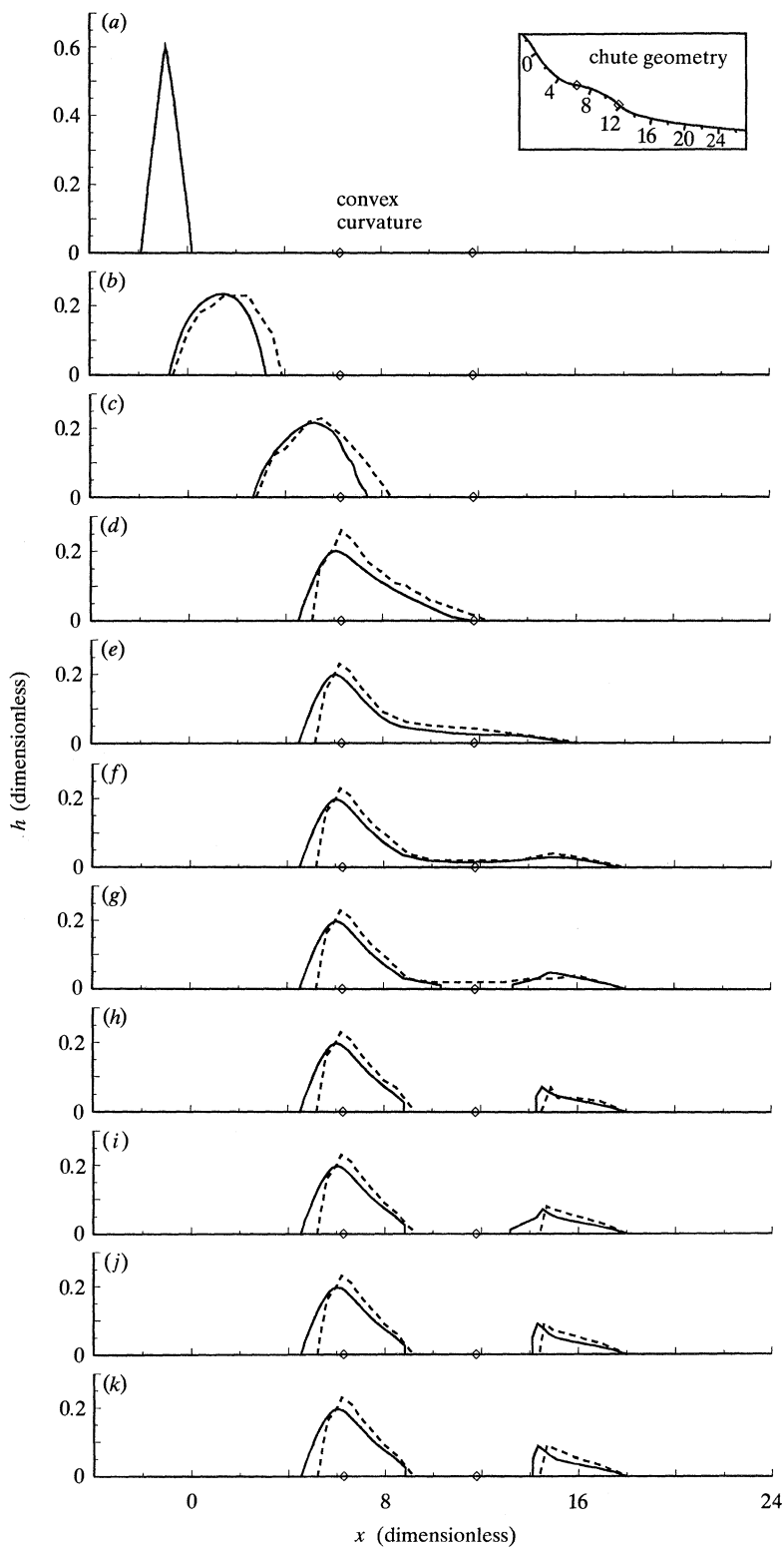
Table 4. *Experimentally and computationally determined ratios of the volumina V_f/V_r of the front and rear depositions in the 16 experiments that were photographed*

no.	$(V_f/V_r)_{exp}$	$(V_f/V_r)_{comp}$
16	0.523 ± 0.06	0.446
17	∞	∞
19	0.574 ± 0.05	
20	∞	21.9
21	∞	10.6
22	∞	3.84
28	0.983 ± 0.08	0.692
29	1.716 ± 0.27	1.32
35	0.345 ± 0.05	0.240
36	0.384 ± 0.08	0.303
37	0.290 ± 0.04	0.340
43	∞	∞
44	0.0576 ± 0.016	0.0518
46	0.136 ± 0.04	0.122
47	∞	∞
48	0.534 ± 0.07	0.441

time. Comparison of the computational solutions with the experimental findings revealed the following results.

1. The theoretical model reproduces the evolution of the granular avalanche as it evolves from the laboratory experiments with good to excellent coincidence. Prerequisite, however, is that $\delta < \phi$ so that the bed can function as a distinct sliding surface (see also Hutter & Koch 1991).

2. Where agreement was less satisfactory it could be explained either by numerical instability (e.g. occasional peaks in the computed $h_s(t)$ function immediately before the avalanche comes to rest) or selection of a rather coarse division of the avalanche pile into cells (necessary for the largest volumes of the avalanches, 3 l, to stabilize the numerical scheme), or an experimental artefact, called 'drizzling' for very roundish granules. In these cases an initially formed deposit in two heaps was slowly eroded from the front end of the deposition above the bump. Final volumes of the experimental depositions below the bump were systematically larger than the corresponding computed ones in these cases.

In short, despite the claims of avalanche practitioners that the Savage & Hutter model may poorly reproduce the experiments in cases when the avalanche track has segments with convex curvature we may conclude that these model equations are appropriate ones if a cohesionless granular material obeying a Coulomb-type internal friction law is moving on a bed with a friction angle that is clearly smaller than the internal angle of friction.

Figure 15. Same as figure 14, but now for experiment no. 36 (1.5 l of quartz 0 on a bed lining made of drawing paper; $\delta_0 = 30°$, $\phi = 44°$, $K_{wall} = 12°$, $N = 40$, $\Delta t = 0.002$, $\mu = 0.05$). (*a*) $t = 0$; (*b*) $t = 2.5$; (*c*) $t = 5.01$; (*d*) $t = 7.60$; (*e*) $t = 10.18$; (*f*) $t = 12.61$; (*g*) $t = 15.20$; (*h*) $t = 17.79$; (*i*) $t = 20.29$; (*j*) $t = 22.88$; (*k*) $t = 24.66$.

References

Anderson, D. A., Tannehill, J. C. & Pletcher, R. H. 1984 *Computational fluid mechanics and heat transfer*. McGraw-Hill.

Greve, R. 1991 Zur Ausbreitung einer Granulatlawine entlang gekrümmter Flächen. Diploma thesis performed on Department of Mechanics, Technological Institute Darmstadt.

Hutter, K. 1991 Two- and three-dimensional evolution of granular avalanche flow – theory and experiments revisited. *Acta Mech.* (Suppl.) **1**, 167–181.

Hutter, K. & Koch, T. 1991 Motion of a granular avalanche in an exponentially curved chute: experiments and theoretical predictions. *Phil. Trans. R. Soc. Lond.* A **334**, 93–138.

Hutter, K., Koch, T., Plüss, Ch. & Savage, S. B. 1992 Dynamics of avalanches of granular materials from initiation to runout. Part II. Laboratory experiments. (In preparation.)

Savage, S. B. & Hutter, K. 1989 The motion of a finite mass of granular material down a rough incline. *J. Fluid Mech.* **199**, 177–215.

Savage, S. B. & Hutter, K. 1991 The dynamics of avalanches of granular materials from initiation to runout. Part I. Analysis. *Acta Mech.* **86**, 201–223.

$t=0$

$t=1.70$

$t=3.32$

$t=4.93$

$t=6.55$
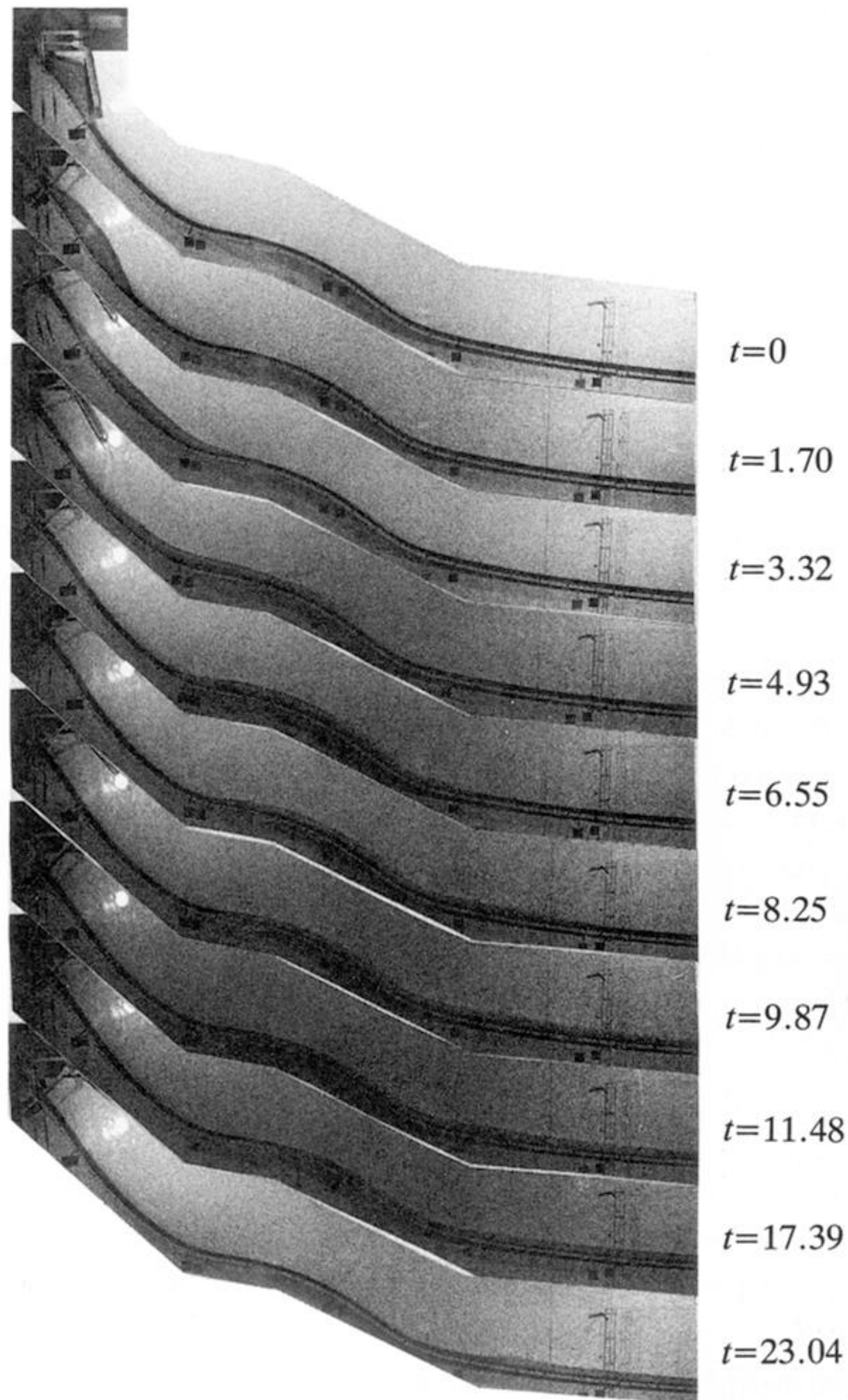
$t=8.25$

$t=9.87$

$t=11.48$

$t=17.39$

$t=23.04$

Figure 3. Series of photographs for experiment no. 20 taken at different dimensionless times of 3 l of glass beads (5 mm diameter) on a bed lined with no. 120 SIA sandpaper moving down the chute defined by equation (3.2).